Preparatory numerical studies for measurements with a confined electron plasma

Titus-Stefan Dascalu

September 18, 2021

Abstract

One critical component of LhARA, The Laser-hybrid Accelerator for Radiobiological Applications, is the Gabor (plasma) lens which is designed to capture and focus the laser-driven proton beam. To understand the experimental limitations in achieving the high density plasmas ($\sim 10^{15}\,\mathrm{m}^{-3}$) required by the design of LhARA, a set of measurements has been planned on the positron beamline in operation at the University of Swansea. This report describes several numerical studies performed in preparation for the measurements. Particle-tracking simulations showed that a low-energy positron beam rotates while passing through a Gabor lens due to the overlap between the external magnetic field and the space-charge field of the plasma. A relation between the plasma density and the angle of rotation of the beam was established. A particle-in-cell (PIC) code was used to simulate the diocotron drift of an off-axis plasma column and to evaluate the expected frequencies for a range of plasma densities, sizes, and amplitudes. For a proper initialisation of the plasma in the PIC simulations, an iterative algorithm was applied to calculate the density distribution of an axisymmetric electron plasma in global thermal equilibrium.

Contents

1 Introduction

One critical component of LhARA, the Laser-hybrid Accelerator for Radiobiological Applications, is the space-charge (Gabor) lens which enables the capture and focusing of the ions produced by the laser-driven source. The Gabor lens uses a non-neutral electron plasma confined in a Penning-Malmberg [1] trap to provide the focusing field for a positively charged beam that passes through the plasma. In the development of LhARA, it is important to prove that such a plasma lens can be operated in a stable regime with the designed focusing strengths. The current design of LhARA [2] employs five lenses, three of which are used to determine the energy selection.

Several plasma instabilities have been observed experimentally to disrupt the ion beam [3–6]. Previous work [7] investigated the origin of the instabilities by using a particle-in-cell (PIC) code, VSim [8], to simulate the dynamics of the non-neutral plasma confined by the lens. For each type of instability observed, its effect on a proton beam was studied by tracking the protons through the electron cloud. Simulating both the plasma and the proton beam with the PIC code is computationally expensive, but achievable. A faster alternative method was devised by generating a time-dependent idealised electric field map to represent the space-charge through which the protons were tracked using BDSIM [9].

A first prototype of a space-charge lens for LhARA was built at Imperial and tested with a proton beam. The initial pencil beams were focused into ring shapes with several distinctive features which suggest that the confined plasma was unstable during the measurements [10]. The formation of the rings was reproduced in simulations with the PIC code and a model of the plasma was created to account for some of the features of the rings [7]. Matching the measurements with the simulations led to an estimation of the plasma densities achieved with the first prototype of the lens. The estimations are an order of magnitude lower than the plasma densities required by the LhARA conceptual design.

Thus, the next stage towards an improved design iteration of the Gabor lens for LhARA has two main aims. The first goal is to validate the simulation software (VSim) that is used to make predictions of the characteristics of the confined plasma (e.g. stability, maximum density, spatial uniformity). The second goal is to better understand the experimental limitations that mean higher electron densities cannot be achieved.

This report presents the initial studies that were done in preparation for the experimental measurements. Section 2 outlines the proposed measurements, each with the corresponding aims and methods. Section 3 describes the particle-tracking simulations done to evaluate whether an observable focusing effect can be achieved by passing a low-energy positron beam through an electron plasma. Section 4 reports the method and results of the particle-in-cell (PIC) simulations that model the diocotron drift of a plasma column.

2 Proposed measurements

This section describes a set of measurements that are planned to be done on the positron beamline at the University of Swansea. The measurements are described starting from two main aims related to the design of a Gabor lens for LhARA and a third, new investigation is also proposed.

Development Firstly, we would like to characterise the capabilities to confine a high density plasma with the storage trap available at Swansea and to identify the factors that limit the maximum achievable density. While the geometry of the storage trap described in subsection 3.1 is similar to the geometry of the Gabor lens proposed for LhARA, the confining fields were designed for lower space charge and, thus, lower plasma densities. Nonetheless, the measurements will allow us to study the total number of stored electrons in relation to the externally applied fields, and to investigate the capability to change the plasma density and the plasma radius by using the rotating-wall (RW) technique [11].

Validation Secondly, some of the measurements will be compared to results from the PIC simulations. The comparison will help us evaluate the suitability of the simulation software and validate it for modelling plasmas confined in a Penning-Malmberg trap. If the main processes in the plasma are accurately covered by the PIC simulations, the corresponding software represents an important tool for making predictions in the next design iteration of the Gabor lens for LhARA.

New measurements Finally, the beamline has been designed for operation with positrons. Thus, it is possible to attempt to take a set of new measurements and study the focusing properties of a confined

electron plasma on a low-energy positron beam.

2.1 Experimental limitations on plasma confinement

The first set of measurements is planned to investigate the experimental limitations of a plasma lens in relation to the focusing properties called for by the design of LhARA. The electron source will be located on axis and a 'beam-catching' technique will be used to fill the storage trap. The aim is to study the total number of electrons that can be trapped for different electrodes used as the end gates and various voltages applied to them. For given conditions, we will use the RW electrode to change the plasma density and radius and investigate the limits on these two plasma parameters. For the design of a lens for LhARA, it is critical to evaluate the upper limit in the electron density. Then, the maximum achievable density can be compared to the Brillouin limit to evaluate the efficiency of the trap. Furthermore, measuring the transverse plasma profiles for a range of plasma lengths and densities will inform us on the uniformity of the plasma and, thus, on the degree of deviation form aberration-free focusing.

2.2 Diocotron motion

The second study is planned to measure the frequency of the diocotron drift of an off-axis plasma column for various electron densities, plasma lengths, plasma radii, and displacements from the axis of the trap. The electron source will be located off-axis and the beam will be captured either by keeping the emission current constant and varying the gate electrodes or by fixing the length of the plasma and varying the emission current. Furthermore, the source will be placed at different displacements, while keeping both the emission current and the gate electrodes fixed. A final option is to compare destructive and non-destructive measurements [12] in view of the instrumentation required by the lens for LhARA. The mapping of the diocotron motion on the MCP/phosphor screen with respect to time will be compared to the non-destructive frequency measurement of induced charges on the segmented electrode, where possible.

2.3 Positron beam focusing

A low-energy positron beam can be obtained on the beamline at Swansea by two methods. If the positrons originate directly from the source, they form a DC beam which propagates on axis. Alternatively, an off-axis AC 'cloud' of positrons can be obtained by accumulating them in the buffer gas trap upstream of the storage trap and, then, releasing the cloud towards the electron plasma in the storage trap. With an on-axis beam, no observable change in the beam radius is expected due to the external magnetic field around the electron plasma. The solution is to measure the angle by which an on-axis elliptical beam rotates as it passes through the electron plasma. A slit collimator can be placed upstream of the storage trap to form an elliptical positron beam.

Alternatively, the electron cloud also induces a change in the position of a thin positron beam that enters the space-charge off axis. Provided that an off axis positron cloud can be ejected toward the storage trap, its change in position can be mapped as a function of the length and density of the electron plasma.

3 Positron beam focusing

3.1 Positron beamline

The positron beamline at Swansea is about 6 m long and comprises the positron source chamber, the buffer gas accumulator, the storage trap, and a laser/target cross.

Source The source chamber contains a 4 K cold finger onto which a positron emitting radioactive source (Na-22) is thermally connected, but electrically isolated via a sapphire disk. Neon is condensed onto the source to moderate the positrons such that $\sim 1\%$ of positrons are emitted with a few eV kinetic energy. The emitted positrons are accelerated downstream by biasing the source to a voltage in the range 50–100 V. Radial confinement of the positrons along the beamline is provided by Helmholtz-like guiding coils of field strength up to 100 G.

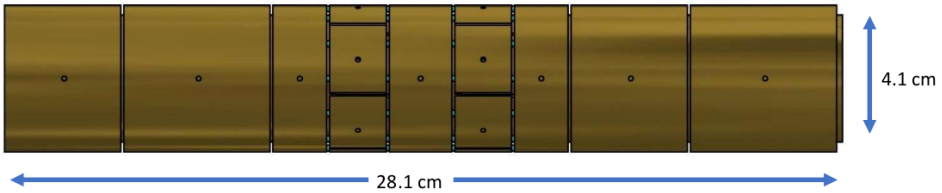

Figure 1: Illustration of the layout of the nine individual bias-able electrodes of the storage trap. Two electrodes are six-way segmented for the application of the rotating-wall (RW) technique [11]

Buffer gas trap The buffer gas trap comprises of 20 cylindrical electrodes immersed in a 400 G solenoidal magnetic field. The electrodes are independently biased to provide an axial trapping profile usually with a low potential barrier at the upstream end of the trap and a higher barrier at the dowstream end. Nitrogen gas is injected and due to the differential pumping and varying electrode conductances, a static pressure profile is established. Carefully choosing the pressure and bias potentials allows positrons to be accumulated. The positrons are manipulated as necessary to increase their number, or density, or control the radial positioning.

Storage trap The storage trap (Penning-Malmberg trap) comprises of nine independently bias-able cylindrical electrodes out of which two are six-way segmented as shown in figure 1. The full length of the trap is 28.1 cm with a diameter of 4.1 cm. The electrodes are immersed in a magnetic field of about 400 G created by a 68 cm long solenoid. Typical operation takes place at a background gas pressure around 10^{-6} mbar. The storage trap can be used for stacking positrons from the upstream buffer gas trap or for trapping an electron plasma. For the latter, an electron source is installed on a linear manipulator upstream of the storage trap. Downstream of the trap, a microchannel plate (MCP) and a phosphor screen assembly is located for imaging the radial position and line integrated density of positrons or electrons.

Operation with electrons For electron plasma studies, the trap is loaded by a 'beam catching' technique as opposed to collision or stream instability. This simpler technique allows the trapping of electron densities $N_z \sim 10^6\,\mathrm{cm}^{-1}$ and typical plasma radii between 0.5 mm and 1 mm. The electron source is made out of a 90 W W-filament that outputs a typical current of 25 µA at 30 V with 1–2 eV spread. Destructive measurements (ejecting the plasma towards the MCP) allow the plasma size, position, total particle number, and plasma temperature to be determined. Optical imaging of the phosphor screen provides position information and determination of the line-integrated density. The screen can be used as an anode to collect an amplified signal from the electrons hitting the MCP. The corresponding signal can be configured to provide timing information or integrated charge (ideal for plasma temperature diagnostics).

Non-destructive measurements are also possible and allow, for example, the diocotron frequency to be determined from the image charges induced in the segmented electrodes. If a charge confined in a Penning-Malmberg trap is located away from the central axis, there will be a defined image charge induced in the conductive walls of the electrodes. If the induced image charge is probed at a specific azimuthal location, a signal can be recorded as a function of time. The signal can, then, be compared to theory and a few plasma parameters determined.

Rotating-wall (RW) technique An important technique for manipulating non-neutral plasmas is to compress the plasma radially using a rotating electric field. This method has been proved to be critical for counteracting outward plasma transport, thus, allowing essentially infinite confinement times [13], and for achieving higher plasma densities [14]. The RW compression involves coupling a rotating electric field to the plasma to inject angular momentum.

For a sufficiently large magnetic field, the total angular momentum of the plasma, P_θ, is dominated by the vector potential contribution over the mechanical contribution and can be approximated by

$$P_\theta \cong \frac{-eNB}{2}\left\langle r^2 \right\rangle, \tag{1}$$

where N is the total number of electrons, and $< r^2 >$ is the mean-square plasma radius. Thus, a radial electric field rotating in the same direction as the plasma will result in compression if the field rotates at a frequency $f_{RW} > f_E$, and expansion of the electrons if $f_{RW} < f_E$. Here, $f_E = en_e/4\pi\epsilon_0 B$ is the plasma $\mathbf{E} \times \mathbf{B}$ rotation frequency. The rotating field typically has a low-order azimuthal mode number (e.g. $m_\theta = 1$) and it is applied through a segmented electrode located at one end of the trap. Good compression is achieved for the axial extent of the segmented electrode less than half the length of the plasma.

Most RW compression experiments today operate in the so-called 'strong drive' regime [15] when the drive amplitude is sufficiently large and the electric field satisfies a 'low-slip' condition

$$\frac{f_{RW} - f_E}{f_{RW}} \ll 1. \tag{2}$$

A broad range of densities have been obtained in this strong-drive regime. It has also been found that, upon the application of the rotating field, the plasma evolves to high density states with $f_E \approx f_{RW}$ that correspond to constant-density rigid-rotor states close to thermal equilibrium [14]. The strong-drive regime can be accessed depending on the ability to overcome the drag due to static asymmetries in the laboratory frame. The drag is a result of these asymmetries driving waves that travel backwards on the rotating plasma. Since these waves have zero frequency in the lab frame, they are referred as 'zero-frequency modes' (ZFM) [14].

One experimental step towards building a reliable Gabor lens is to employ the system at Swansea to test the focusing effect of an electron plasma on a low energy positron beam. The beam can either be DC and obtained directly from the Na-22 source or an AC 'cloud' ejected from the buffer gas trap. In order to evaluate the feasibility of such a set of measurements and the expected observations, a model has been created for the main part of the beamline around and including the storage trap. The model was used to simulate the passage of a positron beam through an idealised electron cloud for various densities and lengths of the confined plasma. While in the absence of a magnetic field the beam is expected to be focused by the space-charge of the plasma the surrounding solenoidal field in combination with the focusing electric field leads to a rotation of the beam without any significant changes of its size.

In the absence of any surrounding magnetic field, a constant density electron plasma represents an ideal beam-focusing element. The space-charge creates a radial focusing field, which under the thin-lens and paraxial beam approximation, can be described by a focal length f which depends on the beam and plasma parameters according to

$$f = \frac{2\epsilon_0\gamma_0 m_p \beta_0^2 c^2}{qe} \frac{1}{n_e L} \tag{3}$$

where m_p, q are the mass and charge of the positron, proton or ion being focused, β_0, γ_0 are the relativistic factors of the positively charged particles in the beam, and n_e and L are the density and length of the electron plasma.

Due to the sizes of the electrodes in the storage trap (see figure 1), four plasma lengths are considered in the following analysis: 2, 5, 9, and 19 cm, all of which can be achieved by individually biasing to a negative voltage a separate pair of electrodes symmetrically positioned with respect to the midplane of the trap. Figure 2 shows the range of achievable focal lengths for several beam and plasma parameters that are typical to the system at Swansea. To focus the low energy positron beam in a region close to the detector, the required electron density is in the range $1 \times 10^{11}\,\mathrm{m}^{-3}$ to $2 \times 10^{12}\,\mathrm{m}^{-3}$ and must be adapted in accordance with the length of the plasma.

3.2 Magnetic field map

While a constant density electron cloud provides a radial focusing force for a positron beam, the presence of the axial magnetic field required to confine the plasma may modify the focusing effect due to the low energy of the positrons. In order to asses the effect of the magnetic field, the coils around the storage trap and the central solenoid have been modelled. The resulting magnetic field map was then used as input to the beam-tracking simulations.

The magnetic field required to confine the electron plasma inside the electrodes shown in figure 1 is provided by a solenoid. Two pairs of steering (quasi-Helmholtz) coils are positioned around the two vacuum crosses immediately upstream and downstream of the solenoid. The parameters of both the main solenoid and the steering coils are given in table 1. The coils and solenoid were simulated using

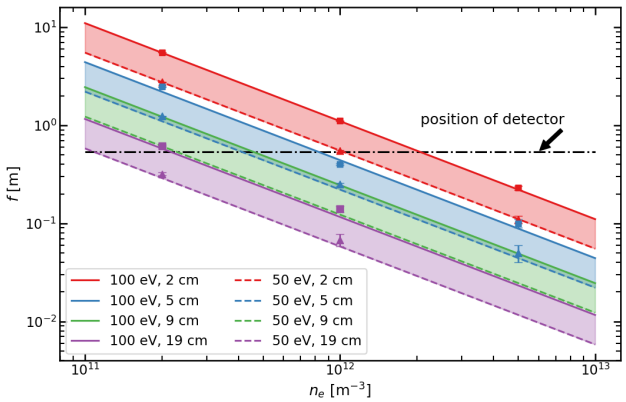

Figure 2: The focal length of a constant density electron plasma for various lengths of the plasma and energy of the positron beam passing through the lens, according to equation (3). Each coloured band shows the range of focal lenths for a fixed plasma length and a beam energy between 50 eV and 100 eV.The detector (MCP) is position approximately 54 cm downstream of the middle plane of lens.

Table 1: Specifications of the magnetic coils and solenoid modelled for the system at Swansea.

Parameter	**Solenoid**	**Steering coils**
Internal diameter [mm]	146	526
External diameter [mm]	162	600
Length [mm]	680	60
I [A]	30	6
Turns	680	400

a finite element analysis package FEMM [16]. The software is used to solve 3D axisymmetric linear magnetostatic problems with a low computational cost. For the studies presented here, the package was used to obtain a 2D axisymmetric magnetic field map starting from the value of the current through the coils and their configuration. The resulting field strength around the beamline is shown in figure 3.

The field map obtained with FEMM was then loaded into BDSIM with the help of a regular grid interpolator and the interface between Python and BDSIM. Figure 4 shows the axial component of the magnetic field on the beam axis from the entrance to the vacuum cross upstream of the storage trap, the main solenoid and the vacuum cross downstream of the trap where the detector is placed. The trap electrodes are placed in the middle of the solenoid, in a uniform field region of about 400 G. The magnetic field outside of the electrodes is not zero due to the steering coils and the two end sections of the solenoid. The evolution of the transverse size of a positron beam propagating through the magnetic field is shown in figure 5.

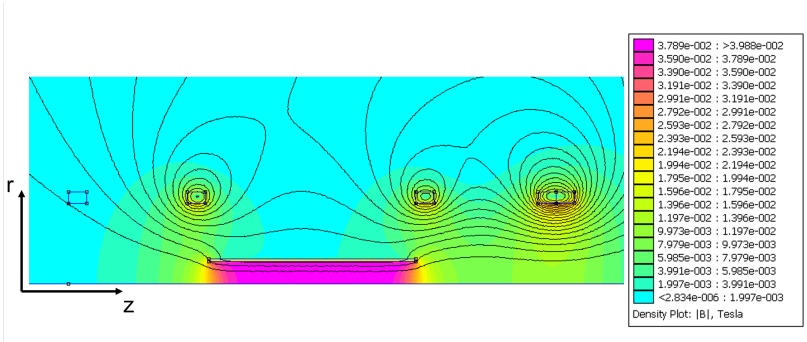

Figure 3: The magnetic field strength and field lines in the (z, r) plane around the positron beamline as obtained with FEMM. The rectangular contours mark the position and size of the two pairs of quasi-Helmholtz coils and the main solenoid in-between.

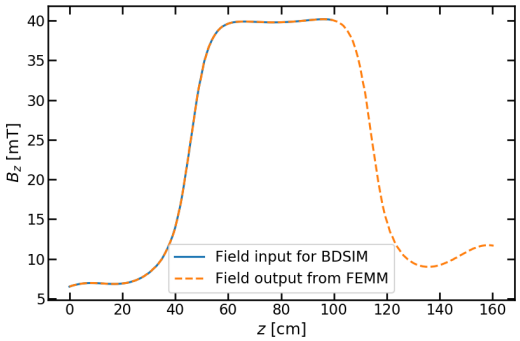

Figure 4: The axial magnetic field strength on the beam axis in the region upstream, inside and downstream the storage trap. The 2D field profile from FEMM is interpolated on a 3D grid and imported into BDSM. The solid line shows the interpolated field only in a partial section of the beamline.

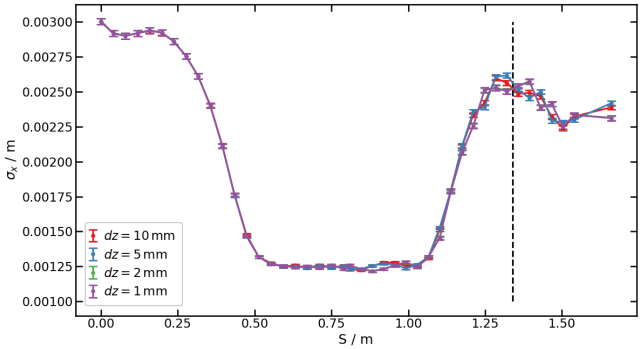

Figure 5: The size of a positron beam that propagates along the magnetic field shown in figure 4 as tracked with BDSIM. The magnetic field map was defined at transverse planes separated by dz. The dashed line indicates the position of the detector (MCP). The beam was propagated through only a magnetic field (no electron cloud).

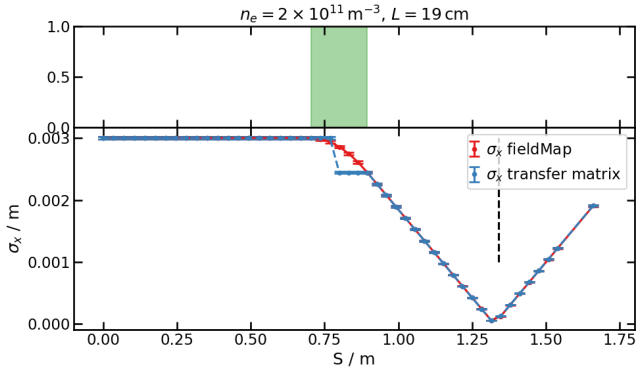

Figure 6: Evolution of the transverse beam size for a positron beam passing through an electron plasma. The space charge was modelled as both a 3D field map or as a transfer matrix for a thin lens. The green region marks the volume filled by the space-charge. A discontinuity is present in the case of the transfer matrix as the transformation is applied in the middle of the element. The beam was propagated through only an electric field (no magnetic fields).

3.3 Electric field map

For the studies described in this section, the electron plasma was modelled as a cloud of uniform charge density that fills the internal volume of the trapping electrodes. For a uniform space-charge, the radial component of the electric field is given by

$$E_r = -\frac{n_e e}{2\epsilon_0} r \tag{4}$$

where n_e is the electron density and r is the radial distance from the central axis of the trap. A 3D electric field map was generated from equation (4). Due to the uniformity of the space-charge along the z axis and assuming a net zero effect of the longitudinal electric field component E_z, the field map had $E_z = 0$ set throughout the entire volume. The electric field map was generated on a uniform 3D grid and a cubic interpolator was used by BDSIM. No difference could be observed when switching between the 'cubic' and the 'nearest' interpolators available in BDSIM. For particle-tracking inside the electron plasma, the maximum step size in the integration was restricted to 2 μm.

Special care was taken to define the field map in a volume that extends longitudinally past the entry and exit plane of the actual electron cloud. While BDSIM uses the field map for particle-tracking only inside the volume of the electron cloud, it was observed that sometimes the field map is not calculated on the entry and exit planes of the electron cloud if the longitudinal extent of the electric field map is the same as the length of the element that represents the space-charge cloud.

To verify the tracking through the generated field map, the optical functions were compared with a separate simulation in which the space-charge cloud was modelled as a transfer matrix that corresponds to a thin lens with the focal length given by equation (3). Figure 6 shows the agreement in the transverse beam size between the two different models of the electron plasma. All the other optical functions showed similar good agreement.

3.4 Single particle trajectories

The first step in studying the focusing effect of an electron plasma on a low energy positron beam under the conditions of a real experiment was to track individual positrons through the electric field of the space-charge combined with the magnetic field from the beamline elements. Several cases were studied for various electron densities and steering coils turned on or off. For each case, three positrons were simultaneously tracked through the beamline with initial offsets from the beam axis of 1, 2, and 3 mm, respectively. The positrons had a kinetic energy of 85 eV. The transverse components of momentum were fixed to an arbitrarily small value of $x' = y' = 10^{-6}$ rad.

Figure 7 shows the axial magnetic field strength along the beamline and the volume occupied by the electron plasma, together with the trajectories of three positrons with different initial transverse offsets. In the regions with only a magnetic field, the positrons undergo cyclotron rotation around the magnetic field lines. The gyroradius can be seen to decrease in the sections with a lower magnetic field strength. In

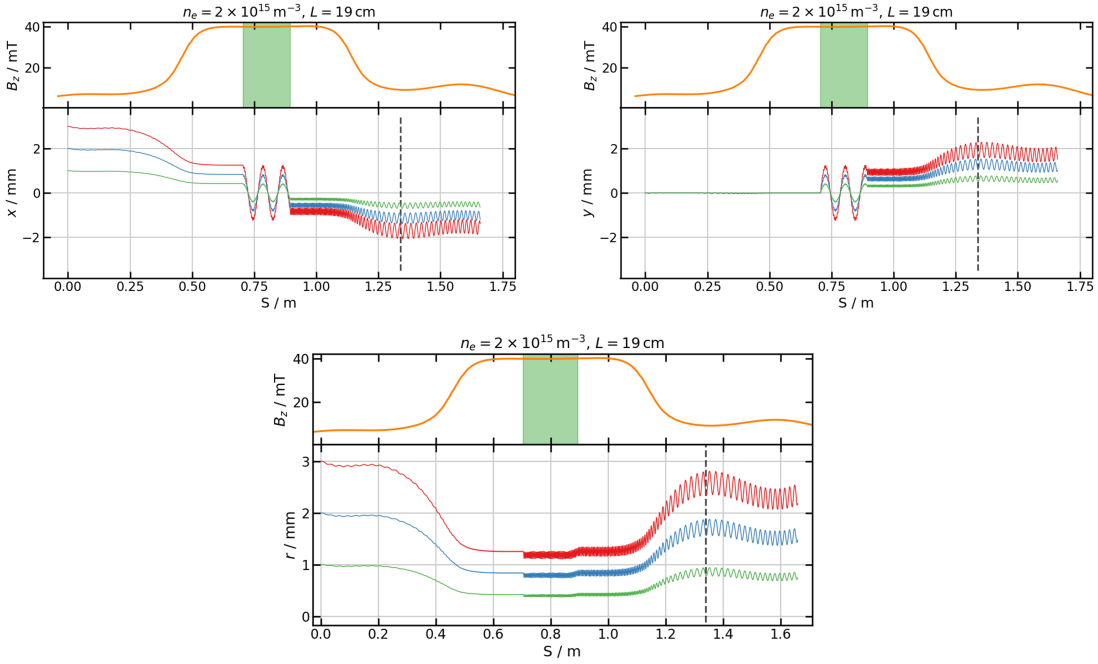

Figure 7: Single particle trajectories for three positrons with initial offset of 1,2, and 3 mm from the beam axis. The top panel of each figure shows the axial magnetic field strength B_z along the beamline and the region filled by the electron plasma in green. The motion in the transverse x and y directions, as well as the change in radius r show a cyclotron rotation of each positron around a guiding centre. The guiding centre itself rotates around the beam axis while passing through the electron plasma. The dashed line marks the position of the detector (MCP).

the region occupied by the electron plasma, the $\mathbf{E} \times \mathbf{B}$ field causes an additional rotation of the guiding centre around the central beam axis, as shown schematically in figure 8.

Assuming that the gyroradius is small such that the changes in the radial component of the electric field can be neglected, the guiding centre of the cyclotron rotation will drift with a drift velocity

$$\mathbf{v_d} = \frac{\mathbf{E} \times \mathbf{B}}{B^2} \tag{5}$$

For a uniform electron cloud, $E \propto r$ implies that $v_d \propto r$. Therefore, the angular velocity of the positrons is independent of their radial position which results in the entire beam rotating around the beam axis as a rigid rotor. The angular velocity increases with the density of the plasma, as can be seen in figure 9 from the increase in the number of full rotations of a positron while passing through the electron cloud.

To verify the results from the single particle-tracking simulation, a separate script was written to numerically integrate the full equations of motion

$$\begin{cases} \ddot{x} = \omega_c \dot{y} - \alpha x \\ \ddot{y} = -\omega_c \dot{x} - \alpha y \\ \ddot{z} = 0 \end{cases} \tag{6}$$

where $\omega_c = eB/m_e$ and $\alpha = n_e e^2 / 2\epsilon_0 m_e$. Figure 10 shows the calculated trajectory in the transverse plane for a positron passing through the storage trap. For the case of $n_e = 2 \times 10^{15}\,\mathrm{m}^{-3}$ and $L = 19\,\mathrm{cm}$, numerically integrating the radial acceleration gives an average radial velocity of approximately $-0.7\,\mathrm{ms}^{-1}$. For a transit time of about $3.5 \times 10^{-8}\,\mathrm{s}$, the numerical result is consistent with the absence of a significant radial drift of the guiding centre which would correspond to beam focusing.

3.5 Positron beam size evolution

In addition to single particles, a beam of positrons was also tracked through the beamline. The beam was defined to be Gaussian with $\sigma_x = \sigma_y = 3\,\mathrm{mm}$, $\sigma_{x'} = \sigma_{y'} = 10^{-6}\,\mathrm{rad}$, a kinetic energy of 85 eV, and no energy spread.

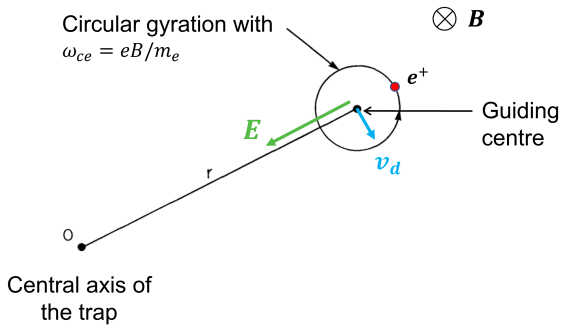

Figure 8: Schematics of the trajectory of a positron in a $\mathbf{E} \times \mathbf{B}$ field. The particle undergoes cyclotron motion around the $\mathbf{B}$ field lines. In a constant radial electric field $\mathbf{E}$, the guiding centre of the circular motion drifts around the central axis with a velocity v_d.

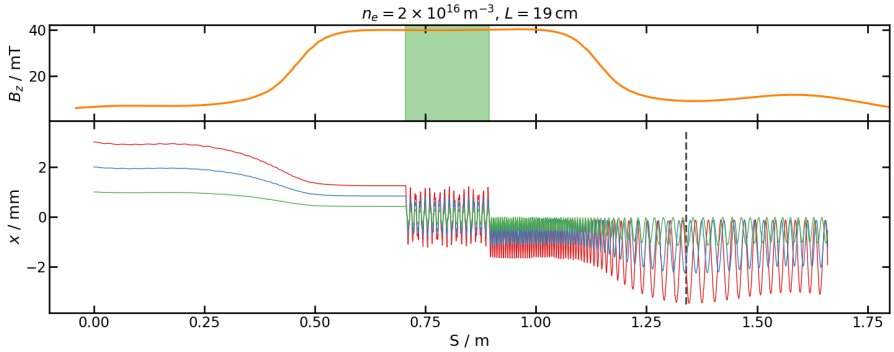

Figure 9: Single particle trajectories in the transverse x direction for three positrons with initial offset of 1,2, and 3 mm from the beam axis. The top panel shows the axial magnetic field strength B_z along the beamline and the region filled by the electron plasma in green. The number of full oscillations inside the plasma increases for higher electron density n_e.

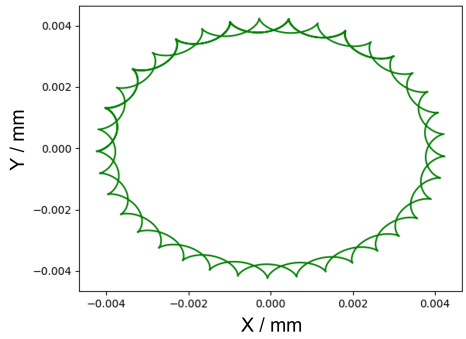

Figure 10: Trajectory in the transverse plane for a positron that passes through the $\mathbf{E} \times \mathbf{B}$ field within storage trap as numerically calculated from equations (6). Due to the short transit time and small radial variations in $\mathbf{E}$, no radial drift of the trajectory can be observed.

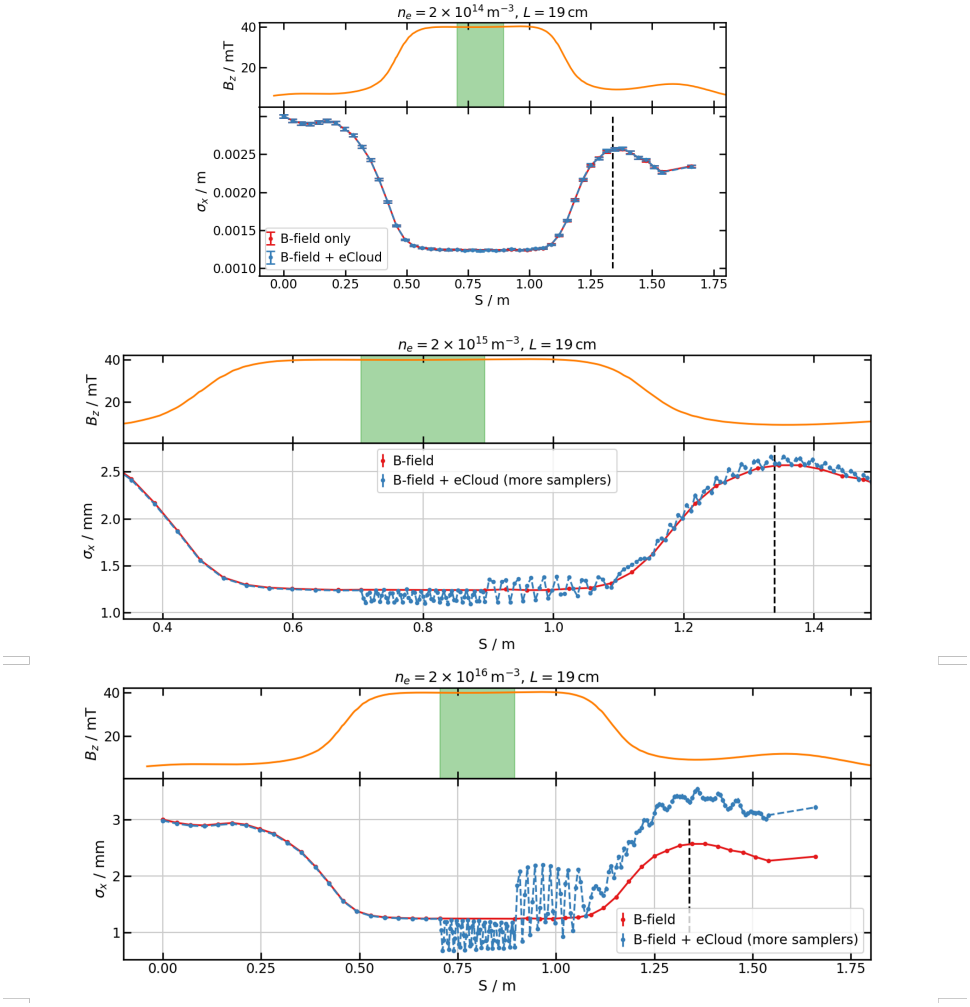

Figure 11: The evolution of the transverse size of a beam of positrons that propagates along the beamline when the storage trap is empty compared to three electron densities of $2 \times 10^{14}\,\mathrm{m}^{-3}$ (top), $2 \times 10^{15}\,\mathrm{m}^{-3}$ (middle), and $2 \times 10^{16}\,\mathrm{m}^{-3}$ (bottom). An observable change in the beam size appears at the highest density. Due to the small separation of the planes at which the beam size is sampled, the faster change in the beam size due to the cyclotron rotation of the positrons can also be observed.

Figure 11 shows how the size of the positron beam changes throughout the electron plasma and downstream of it up to the position of the detector. For an electron density below $2 \times 10^{15}\,\mathrm{m}^{-3}$, no significant change in the beam size was observed. For higher density, $2 \times 10^{16}\,\mathrm{m}^{-3}$ and above, the beam size is larger at the position of the detector compared with the case of no plasma in the storage trap. The increase in the beam size at relatively high plasma densities is caused by the high amplitude oscillations of the beam size inside the electron cloud which perturbs the cyclotron motion of individual positrons downstream of the plasma. A mono-energetic beam passing through an ideal lens has a well-defined focal point where the beam size is infinitesimal. Even though the beam energy spread is zero, the beam size never reaches a value close to 0 mm. This is an indication of the absence of focusing. This result suggests that, even at relatively high plasma densities, a focusing effect on the positron beam would not be observed. By comparison, in the absence of a magnetic field, a plasma with a density around $10^{14}\,\mathrm{m}^{-3}$ should focus a low energy beam in a space shorter than 1 cm (see figure 2).

Furthermore, figure 11 also shows several oscillations of the beam size inside the plasma which can be explained by the cyclotron motion of the positrons. The effect of the cyclotron motion of individual positrons on the beam size is visible due to the small separation between the planes at which the beam size was sampled. Due to the large cyclotron frequency and low beam energy, the positrons execute several gyrations during the transit time through the plasma.

3.6 Positron beam rotation

Based on the absence of an observable focusing effect that was discussed above, a second experimental observable can be represented by the rotation angle of an elliptical positron beam. It was argued previously that the positrons in the beam rotate with the same angular velocity which is determined by the plasma density and the solenoidal field. To verify this statement, an elliptical positron beam was tracked through the beamline and its orientation in the xy plane was sampled at several illustrative locations.

Figure 12 shows how the orientation of a Gaussian elliptical beam that starts with $\sigma_x = 3\,\mathrm{mm}$, $\sigma_y = 0.5\,\mathrm{mm}$, and the major axis parallel to the x direction, changes through the beamline. At the entry plane of the plasma, the beam has been focused due to the density of the magnetic field lines increasing upstream of the storage trap. Through the plasma, the beam rotates as a rigid object by almost two and a half full rotations. Between the exit plane of the plasma and the detector, the beam expands due to the decrease in the magnetic field strength. However, the rotation angle with which the beam exits the plasma is preserved up to the detector.

From the equations (4) and (5), one can obtain a new expression for the angle by which the beam rotates between the entry and exit planes of the plasma

$$\Delta\theta = \frac{e n_e L}{2\epsilon_0 B v_{\mathrm{beam}}} \tag{7}$$

where v_{beam} is the velocity of the positrons in the beam and L is the length of the plasma. Figure 13 shows the amount by which the beam rotates within the electron plasma for three different positron energies, 50, 85, and 100 eV, as a function of the figure of merit $n_e L$. The simple model of equation (7) agrees well with the beam-tracking simulations performed using BDSIM. The region of interest with rotation angles between about 0.02 rad and π rad corresponds to $4 \times 10^{11}\,\mathrm{m}^{-2} \lesssim n_e L \lesssim 5 \times 10^{13}\,\mathrm{m}^{-2}$. In the treatment above, the beam was considered to be relatively large and to enter the beamline on the beam axis. The same results apply for a thin pencil beam that starts to propagate with a radial offset. The final position of the pencil beam will be rotated by an equivalent angle also given by equation (7).

The beam-tracking simulation was also used to look at the correlation between the angle by which the beam rotates through the electron plasma and the rotation angle which can be measured at the position of the detector relative to the orientation of the beam at the start of the beamline. Figure 14 indicated that a good correlation exists only for relatively large angles above approximately 0.2 rad. For lower angles, the beam rotation angle measured at the detector is less than the amount by which the beam rotates by passing through the plasma. This is a result of the rotation of the beam inside the plasma being smaller or comparable to the rotation caused by the propagation through the rest of the beamline.

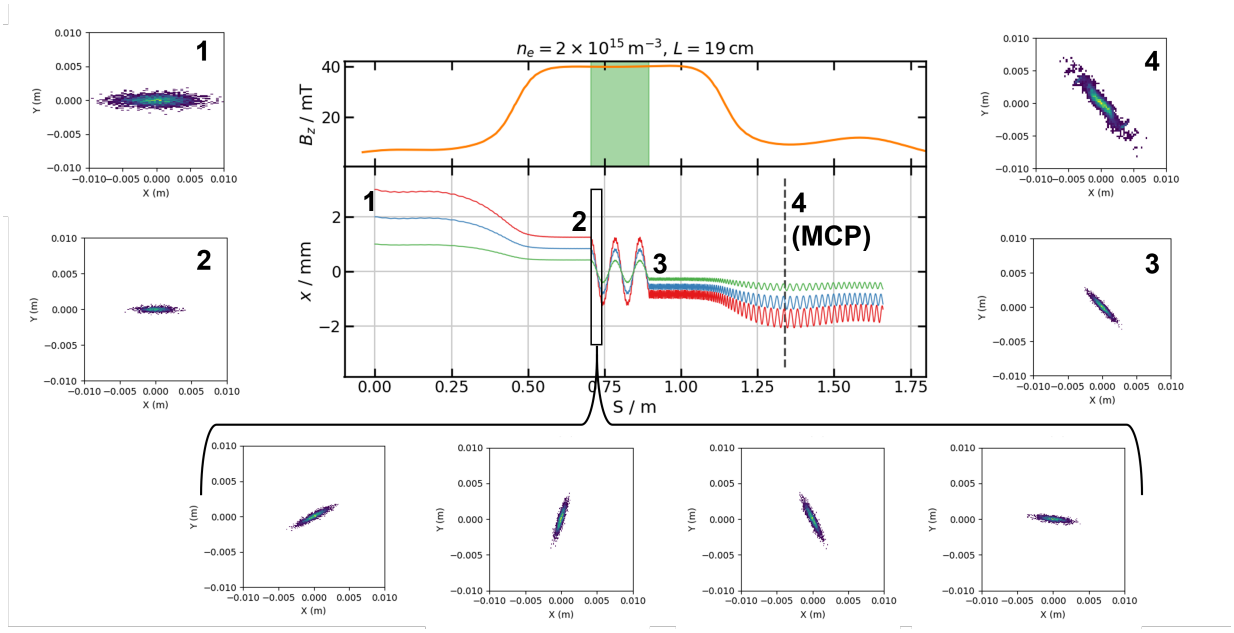

Figure 12: Summary of single particle- and full beam-tracking results. The trajectory of individual positrons are shown with the red, blue, and green lines. The lateral panels show the orientation of an elliptical positron beam at various key locations in the beamline: 1–start of the beamline, 2–entry plane of the plasma, 3–exit plane of the plasma, 4–position of the detector. The four insets on the bottom show the rotation of the beam in the first approximately 4 cm of the plasma.

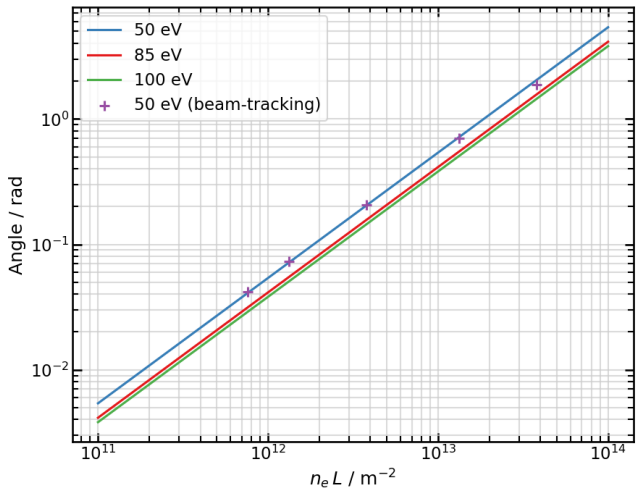

Figure 13: The angle by which a beam of positrons rotates while passing through an electron plasma of density n_e and length L for a beam energy of 50, 85, and 100 eV. The solid lines show the result of the simple model of equation (7). The crosses show the rotation of an elliptical positron beam through a uniform electron plasma according to beam-tracking simulations in BDSIM.

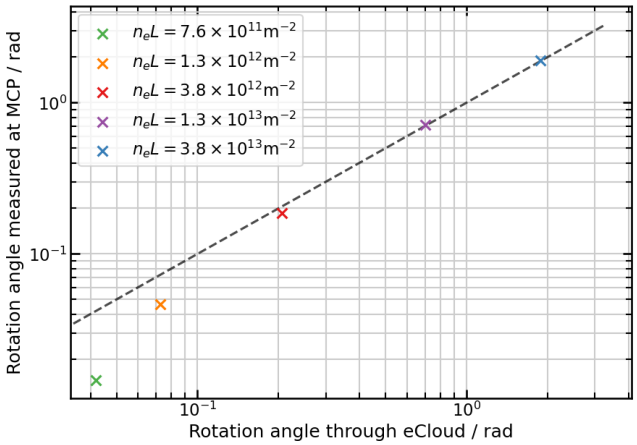

Figure 14: The correlation between the angle by which a positron beam rotates through the electron cloud and the rotation angle measured at the position of the detector (MCP) compared to the start of the beamline. The dashed line marks the 1:1 correlation. The data points were obtained by beam-tracking in BDSIM.

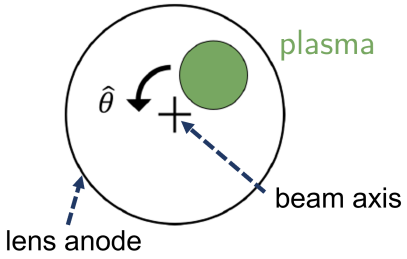

Figure 15: Schematic representation of the $m = 1$ plasma diocotron mode [17] viewed along the axis of the lens.

4 Diocotron motion

4.1 Background theory

In a Penning-Malmberg trap, the electron plasma column experiences an $\mathbf{E} \times \mathbf{B}$ rigid rotation about its axis due to the self space-charge field. If the plasma column is located away from the central axis of the trap, an image charge is induced in the conducting walls of the confining electrodes. The electric field from the image charge results in an additional $\mathbf{E} \times \mathbf{B}$ drift of the plasma which leads to the diocotron rotation (see figure 15). When the azimuthal wavenumber m is not explicitly given, the diocotron motion refers to the fundamental $m = 1$ mode. If the particles bounce axially on a timescale much smaller than the perpendicular drift timescale, the mode corresponds to a rigid-rod plasma that moves on a circular trajectory about the symmetry axis of the trap [18]. Theoretical predictions of the diocotron mode frequency have been obtained under a variety of assumptions.

The analysis started with the simple assumption that the plasma column represents an infinitely long line of charge with infinitesimal radial extent. The image charge is located at $r_i = R_w^2/D$, where R_w is the radius of the wall and D is the amplitude of the mode or the displacement of the plasma from the central axis of the trap. The electric field from the image line charge at the plasma column is uniform and causes the column to orbit around the trap axis at a frequency given by the following full nonlinear formula [18] (cgs units)

$$f_\infty = f_1 \left[\frac{1}{1 - (D/R_w)^2} \right] \tag{8}$$

where f_1 is the linearized infinite-length diocotron frequency

$$f_1 = \frac{cNe}{\pi BLR_w^2} \tag{9}$$

Note that f_∞ is independent of the radial density profile of the plasma column.

However, when D becomes large (i.e. as $D/R_w \to 1$), the image charge approaches the column and the finite radius of the column becomes important due to the field variations across the plasma. The problem has been solved to order $(D/R_w)^2$ for constant density columns by considering the quadrupole perturbation of the plasma profile [19]. The resulting formula for the diocotron mode frequency f_{NL} is valid for finite plasma radius R_p and has a dependence on the amplitude D due to the nonlinear distortion of the column into an elliptical cross-section

$$f_{NL} = f_\infty + f_\infty \left[\frac{1 - 2\left(R_p/R_w\right)^2}{\left[1 - \left(R_p/R_w\right)^2\right]^2} \left(\frac{D}{R_w}\right)^2 \right] \tag{10}$$

Finally, one may relax the assumption that the plasma is infinite in the axial extent. In this case, the diocotron frequency gets two shifts, one due to the finite extent of the image charge, and another due to the force on the plasma ends caused by the electric fields from the axial confinement potentials of the trap [18]. The former contribution f_i, due to the finite length of the image charge, becomes important when the assumption $R_w/L \ll 1$ breaks down. The latter contribution f_c, due to the end confinement fields, must be considered when the assumption $|\Phi_p|/|V_c| \ll 1$ is invalid [18], where Φ_p is the plasma potential and V_c is the confinement voltage.

The image field produces a correction $\Delta f_i < 0$, and the confinement field gives a contribution $f_c > 0$. The problem has been solved [17] to lowest order in $D/R_w, R_p/R_w, R_w/L$, and $|\Phi_p|/|V_c|$. The resulting formula for the small amplitude finite length diocotron frequency is $f_d = f_1 + \Delta f_i + f_c$ where the frequency shifts are

$$\Delta f_i = -0.671 f_1 \left(\frac{R_w}{L}\right) \tag{11}$$

$$f_c = f_1 \frac{j_{01}}{2} \left[\frac{1}{4} + \ln\left(\frac{R_w}{R_p}\right) + \frac{TL}{Ne^2}\right] \left(\frac{R_w}{L}\right) \tag{12}$$

where $j_{01} = 2.405$ is the first zero of the J_0 Bessel function. For a uniform density column, the plasma kinetic pressure term can be approximated as $TL/Ne^2 \approx 4\lambda_D^2/R_p^2$ which gives a less important contribution when the column is a "plasma", i.e. when $\lambda_D \ll R_p$ [17].

4.2 PIC simulations

Modelling simulations were carried out with VSim [8], a software application specially optimised for plasma simulations and designed to run in parallel on high performance computing systems. VSim employs the particle-in-cell (PIC) method. Macro-particles are used to model the dynamics of a discrete number of real particles, electrons in this case. The macro-particles are advanced in time according to the Lorentz equation. In-between the time steps, the charge density is calculated via interpolation of the macro-particles onto a mesh. The charge density is, then, used to calculate an electrostatic potential by solving Poisson's equation. Particle collisions were not modelled due to the collision time scale being much larger than the diocotron period. Due to the diocotron drift of the plasma column in the azimuthal direction, a three dimensional simulation has to be employed.

The electrostatic field solver is applied to an xyz Cartesian grid with constant potential boundary conditions (Dirichlet conditions) at the walls of the electrodes. VSim does not yet include a 3-D cylindrical solver. The Dirichlet conditions are suitable here because they implicitly model the effect of the image charges. By fixing the value of the potential on the metallic surfaces, the transverse electric field is fixed to zero, as it is the case in a real conductor due to the rearrangement of the free electrons. The image charges are not modelled in the simulation, but their effect is implicitly included by solving Poisson's equation with the appropriate boundary conditions.

The geometry of the storage trap, as well as the magnitudes of the magnetic field and electrostatic potentials, are consistent with the experimental setup at Swansea. The parameters with the largest influence on the result of the simulations are discussed below.

4.2.1 Time step

To properly resolve the motion of a charged particle in a magnetic field, the time step should be smaller than the cyclotron period given by

$$\tau_c = \frac{2\pi m}{qB} \approx 3.57 \times 10^{-11} \frac{1}{B\,[\mathrm{T}]} \quad [\mathrm{s}]. \tag{13}$$

Typically, due to the high magnetic field and small gyroradius, the motion of a particle in a PIC simulation is close to a guiding centre motion, in which case the small scale rotation of the particle around a magnetic field line is not fully resolved. Thus, larger time steps result in significant plasma heating.

Another natural time scale for the collective phenomena of interest in a plasma is the inverse plasma frequency ω_{pe}^{-1}. For a stable solution, $\Delta t \omega_{pe}^{-1} < 2$ is required. In the absence of other constraints, the use of a more restrictive time step $\Delta t = 0.2\omega_{pe}^{-1}$ is typically used to give sufficiently accurate results [20]. The above restriction on the time step is associated with the use of an explicit solver, a scheme that advances particles based on old forces from the previous time step. While explicit solvers are simpler and faster, an implicit scheme which uses a new field at the next time step to update particle velocity, requires a much smaller number of time steps.

A further constraint on the time step is set by the Courant–Friedrichs–Lewy (CFL) condition. For an electrostatic simulation, the effective CFL condition requires that a macro-particle moves at most one cell during a single time step. Hence, higher energy particles require smaller time steps. If a maximum temperature or a maximum thermal velocity $v_{\mathrm{th,max}}$ is defined, the CFL condition can be satisfied by setting up the time step according to the following minimum

$$\min\left\{\frac{2}{\omega_{pe}}, \frac{1}{v_{th,max}\sqrt{1/\Delta x^2 + 1/\Delta y^2 + 1/\Delta z^2}}\right\}, \tag{14}$$

where $\Delta x, \Delta y, \Delta z$ are the cell dimensions along each of the x, y, z directions. The size of the time step is the defining factor in the total running time required for a simulation to finish for a fixed number of available CPUs.

4.2.2 Mesh size

In the PIC model, the short-range forces are only approximately modelled since their length scale is of the same order as the size of the mesh. This approximation and the discrete mesh lead to numerical heating and non-conservation of the total energy. However, the degree of numerical heating was observed to decrease by a comparable factor to the decrease in the cell size [21].

Simulations were carried out on a discrete Cartesian mesh with a transverse cell size $\Delta x = \Delta y$ and a longitudinal cell spacing Δz. The natural length scale in an electron plasma is given by the Debye length

$$\lambda_D = \sqrt{\frac{\epsilon_0 k_B T_e}{n_e e^2}} \approx 7.43 \times 10^6 \sqrt{\frac{T_e\,[\mathrm{eV}]}{n_e\,[\mathrm{m}^{-3}]}} \quad [\mathrm{mm}], \tag{15}$$

which represents the upper limit for the mesh size in any direction. This condition adds to the difficulty of simulating a plasma with a low temperature T_e or a high density n_e.

Another length scale which is relevant for an electron moving in a magnetic field is the gyroradius (Larmor or cyclotron radius) ρ_c defined as

$$\rho_c = \frac{m_e v_\perp}{eB} \approx 2.38 \times 10^{-3} \frac{\sqrt{T_e\,[\mathrm{eV}]}}{B\,[\mathrm{T}]} \quad [\mathrm{mm}], \tag{16}$$

where $v_\perp$ is the component of the velocity perpendicular to the magnetic field B. However, in a typical PIC simulation, the gyroradius scale is much smaller than the scale of the Debye length and it is not properly resolved. Thus, the particle motion is treated as a guiding centre motion.

4.2.3 Confinement fields

The maximum density of a plasma confined in a Penning-Malmberg trap is restricted by two conditions necessary to limit the expansion of the plasma in the radial and axial directions, respectively. The first

condition is the Brillouin limit which gives the maximum density n_B that can be confined by a uniform magnetic field B as [22]

$$n_B = \frac{\epsilon_0 B^2}{2m_e} \approx 4.8 \times 10^{18} \left(B\,[T]\right)^2 \quad [\mathrm{m}^{-3}]. \tag{17}$$

The second limit is given by the space-charge potential built up by the confined plasma. The voltage applied to the end electrodes has to be larger than the space-charge potential to ensure axial confinement. For a long, uniform, and cylindrical electron plasma confined with cylindrical electrodes that fully fills the trap at the Brillouin limit, the space-charge potential on the axis of the plasma is calculated as [21]

$$\phi_0 = -\frac{e n_e R_p^2}{4\epsilon_0}\left(1 + 2\ln\frac{R_w}{R_p}\right) \approx 2.2 \times 10^{10} \left(B\,[\mathrm{T}]\,R_p\,[\mathrm{m}]\right)^2 \quad [\mathrm{V}]. \tag{18}$$

Thus, high-density single-component plasmas require substantial voltages to confine them, unless R_p is small. In practice, when the space-charge potential of the plasma is not too high, the voltage applied to the end electrodes is typically $\sim 5 \times \phi_0$.

4.2.4 Electron collision rate

Non-neutral plasmas in a regime away from the Brillouin density limit satisfy the condition $\lambda_D > \rho_c$. In such a regime, when two electrons collide, their momentum vectors scatter. As a result, the guiding centre of each particle moves to a different position and leads to diffusion. Electron-electron Coulomb collisions occur at a rate given by the following formula [13]

$$\nu_{ee} = \frac{16}{15}\sqrt{\pi}\frac{n_e e^4}{T_e^{3/2} m_e^{1/2}} \ln\left(\frac{\rho_c T_e}{e^2}\right), \tag{19}$$

where cgs units are used and the temperature T_e has units of energy. Physically, ν_{ee} is the rate at which a thermal electron loses half of its momentum to other electrons [13]. Equation (19) is equivalent to

$$\nu_{ee} \approx 1.6 \times 10^{-6} \frac{n_e\,[\mathrm{cm}^{-3}]}{T_e^{3/2}\,[eV^{3/2}]} \ln\left(6.9 \times 10^6 \rho_c\,[\mathrm{cm}]\,T_e\,[\mathrm{eV}]\right) \quad [\mathrm{Hz}]. \tag{20}$$

For example, a plasma with a density of the order $1 \times 10^9\,\mathrm{cm}^{-3}$, temperature 0.1 eV and confined by a field with $B = 0.003\,\mathrm{T}$ has an electron-electron collision rate $\nu_{ee} \approx 0.5\,\mathrm{MHz}$.

4.3 Plasma initialisation

In an experiment, there are several techniques by which to capture electrons inside a Penning-Malmerg trap and form a confined plasma. However, since the time scales involved in the capture processes (e.g. electron collision period, axial bounce period, or stream instability rise time) are much larger than the plasma time scales (e.g. plasma period, cyclotron period, or diocotron period), it is computationally too expensive to simulate the capture of electrons. The alternative is to initialise the electrons as a confined plasma directly.

Due to the influence of the transverse density profile of the plasma column on the diocotron mode frequency, the plasma has to be initialised in the simulation as close as possible to the actual stable state both in terms of the spatial density profile and the corresponding velocity distribution. Thus, one can avoid an initial transient phase in the simulation during which the plasma column changes from the initial configuration to a more stable state and also avoid numerical heating of the electrons. Simply initialising the plasma with a uniform density has been observed in simulations to lead to an initial period of time required for the plasma to relax into a new stable state by typically expanding in the radial direction and contracting axially. Figure 16 shows an example from a simulation where the uniform initial plasma column relaxed into a significantly different longitudinal profile.

One way to initialise the plasma closer to the stable state is to assume that for small radial displacements of the column from the trap axis, the density distribution is not significantly different from the distribution of a plasma column in thermal equilibrium and with no offset from the symmetry axis. The reasoning behind this approach is that the equation which determines cylindrically symmetric non-neutral plasma equilibria of this kind have been extensively studied [23–25] and can be computed numerically.

A numerical procedure has been constructed to compute the electrostatic equilibrium of a non-neutral plasma in a uniform magnetic field by solving Poisson's equation using an iterative method. The plasma

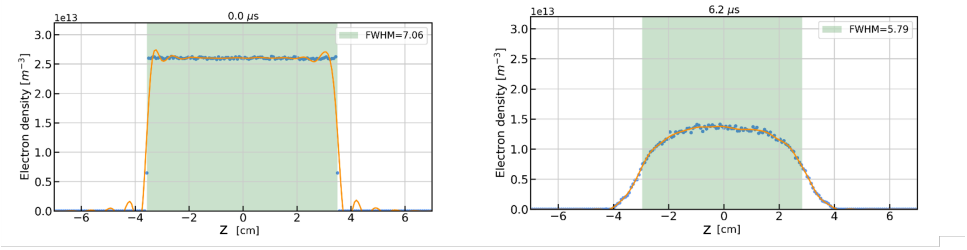

Figure 16: Electron density of the plasma column in the longitudinal direction at 0.0 μs and 6.2 μs. The uniform density changes into a slowly varying profile due to the shape of the confining field. The orange line is a spline fit of the points from simulation to guide the eye.

is assumed to be in a global thermal equilibrium, as described by [25, 26] and [24]. The class of equilibria considered here corresponds to a rigid rotation of the plasma about the axis of symmetry with angular velocity $\omega_{re} = \text{const.}$, for which Poisson's equation has the form

$$\nabla^2\phi = \frac{e}{\epsilon_0} n_e(r,z) = f(r,\phi) \tag{21}$$

In this equation, ϕ is the electrostatic potential and $n_e(r,z)$ is the electron density. The right-hand side of equation (21) takes the form [24]

$$f(r,\phi) = \frac{e\hat{n}_e}{\epsilon_0} \exp\left\{-\frac{m_e}{2k_BT_e}\left[r^2\left(\omega_{re}\omega_{ce} - \omega_{re}^2\right) - \frac{2e}{m_e}\left(\phi - \phi_{00}\right)\right]\right\} \tag{22}$$

where $\hat{n}_e$ and ϕ_{00} are the electron density and potential at the centre of the plasma, T_e and m_e are the electron temperature and mass, respectively, and ω_{ce} is the electron cyclotron frequency. For the choice of distribution function in equation (22) and for the entire class of rigid-rotor equilibria, the plasma column is radially confined ($n_e(r \to \infty, z = 0) = 0$) provided [24]

$$\omega_{ce}\omega_{re} - \omega_{re}^2 - \omega_{pe}^2/2 > 0, \tag{23}$$

where $\omega_{pe} = \sqrt{\hat{n}_e e^2/m_e\epsilon_0}$ is the plasma frequency. Equation (23) is equivalent to $\omega_{re}^- < \omega_{re} < \omega_{re}^+$, where ω_{re}^+ and ω_{re}^- are the cold-fluid rotation velocities given by the two roots of the quadratic equation associated to the inequality (23). If ω_{re} is closely tuned to either ω_{re}^+ or ω_{re}^-, the density profile $n_e(r)$ is uniform and equal to $\hat{n}_e$ over the main radial extent of the plasma column out to some radius $r \gg \lambda_D$, and then $n_e(r)$ falls off abruptly over a distance of a few times λ_D. This is a result of the electrons adapting their position in the equilibrium state to cancel out any externally imposed electrostatic field. On the other hand, if ω_{re} is well removed from the cold-fluid rotation velocities ω_{re}^+ and ω_{re}^-, then the density profile $n_e(r)$ is bell-shaped and it typically extends a few times the Debye length λ_D in radial size [24].

However, in an experiment, it is the radial profile of the plasma column that is most commonly measured, and not the angular velocity ω_{re}. Thus, it is convenient to specify a different quantity r_p from a measured density distribution, where r_p is defined as the radius in the midplane, $z = 0$, at which the plasma density has fallen to half of its central value. The function (22) can, then, be rewritten as [27]

$$f(r,\phi) = \frac{e\hat{n}_e}{\epsilon_0} \exp\left[\frac{e}{k_BT_e}\left(\phi - \phi_{00}\right) - \alpha r^2\right], \tag{24}$$

with the constant α readjusted at each step of the iteration according to the formula

$$\alpha = \frac{e}{k_BT_e r_p^2}\left(\phi(r_p,0) - \phi_{00}\right) + \frac{\ln 2}{r_p^2}. \tag{25}$$

The cylindrical geometry used for computing the plasma equilibria has a radial extent a and a length b, and it is subdivided into rectangular cells with sides of length Δr and Δz. For accurate results, the size of the cell in each of the two dimensions has to be less than or equal to half the Debye length [27]. The plasma was assumed to be axisymmetric and the confining magnetic field uniform and parallel to the axis of the trap. Two ring-shaped end electrodes create the axial confining potential. The computation

region was chosen for a plasma state with reflection symmetry about $z = 0$. Under these conditions, the corresponding boundary conditions on ϕ are

$$\frac{\partial \phi}{\partial r} = 0 \text{ at } r = 0; \tag{26}$$

$$\frac{\partial \phi}{\partial z} = 0 \text{ at } r = z; \tag{27}$$

$$\phi = 0 \text{ at } z = b. \tag{28}$$

Also, at the conducting wall $\phi = \phi(a, z)$ is zero except at the location of the confining electrode.

The iterative method chosen here is successive over-relaxation (SOR) with finite-differences and Newton's method (Newton SOR). This particular iteration scheme was chosen for its simplicity and effectiveness in the present problem [27, 28]. The computation volume is divided into a regular grid and central-differencing is employed to evaluate the derivatives. The solutions are found by relaxation from an arbitrary initial potential $\phi^{(0)}(r, z)$ by progressive iterations over the entire grid. During each iteration, the a new electrostatic potential is obtained at each grid point through

$$\begin{aligned}\phi^{(l+1)}(r,z) =& (1-\omega)\phi^{(l)}(r,z) + \frac{\omega}{2}\left(\frac{1}{\Delta r^2} + \frac{1}{\Delta z^2} + 2\left.\frac{\partial f}{\partial \phi^{(l)}}\right|_{r,z}\right)^{-1} \\ &\times \left[\frac{(1+\Delta r/2r)\phi^{(l)}(r+\Delta r,z) + (1-\Delta r/2r)\phi^{(l+1)}(r-\Delta r,z)}{\Delta r^2}\right. \\ &+ \frac{\phi^{(l)}(r,z+\Delta z) + \phi^{(l+1)}(r,z-\Delta z)}{\Delta z^2} \\ &\left. - f\left(r,\phi^{(l)}(r,z)\right) + \left.\frac{\partial f}{\partial \phi^{(l)}}\right|_{r,z}\phi^{(l)}(r.z)\right],\end{aligned} \tag{29}$$

where $1 < \omega < 2$ is a mixing constant. A good estimate for the best value of ω is the value used to solve Poisson's equation with homogeneous Dirichlet boundary conditions on a rectangular $n_r \times n_z$ grid [29]:

$$\omega = \frac{2}{\sqrt{1-\rho^2}} \tag{30}$$

$$\rho = \frac{\Delta z^2 \cos(\pi/n_r) + \Delta r^2 \cos(\pi/n_z)}{\Delta z^2 + \Delta r^2}. \tag{31}$$

To reduce the total number of iterations required to achieve convergence, ω is updated after each full sweep over the grid according to the Chebyshev acceleration method [29].

The right-hand side of equation (29) contains a mix of iteration levels (both l and $l+1$) to make use of the updated values of ϕ as soon as they become available [27]. Furthermore, the $\partial f/\partial \phi$ term improves the algorithm for nonlinear problems by evaluating $f(r, \phi)$ at the $(l+1)$ iteration level. The potential ϕ is updated starting from the lower left-hand corner of the grid and the calculation proceeds radially first. The iterations are continued until the solution converges within the desired tolerance. It was typically observed that the error grows by a factor of 20 before convergence sets in.

Figure 17 shows the result of computing the density distribution of an electron plasma in a Penning-Malmberg trap with the scheme described in this section. The radial plasma profile has an approximately flat region near the central axis and falls off over a distance of a few times the Debye length. At the end of the half-column, the density also decreases smoothly following the shape of the field lines determined by the confining potential.

Figure 18 shows a comparison between the radial profile extracted from the 2-D calculation of the electron density and a solution to the 1-D problem that corresponds to an infinitely long plasma column. The 1-D solution has been obtained by solving a self-consistent 1-D Poisson equation for an axisymmetric plasma column that undergoes rigid rotation [24, 26]. The same density, temperature, radius r_p, and confining field were used in the 1-D problem as in the 2-D case. The two calculations resulted in highly similar density profiles for long enough plasma columns. The agreement is within 1% for 5 grid points or more per Debye length along each direction.

Once the stable density distribution of the plasma has been computed, the second step of the initialisation procedure is to define the corresponding velocity distribution. For an electron plasma at

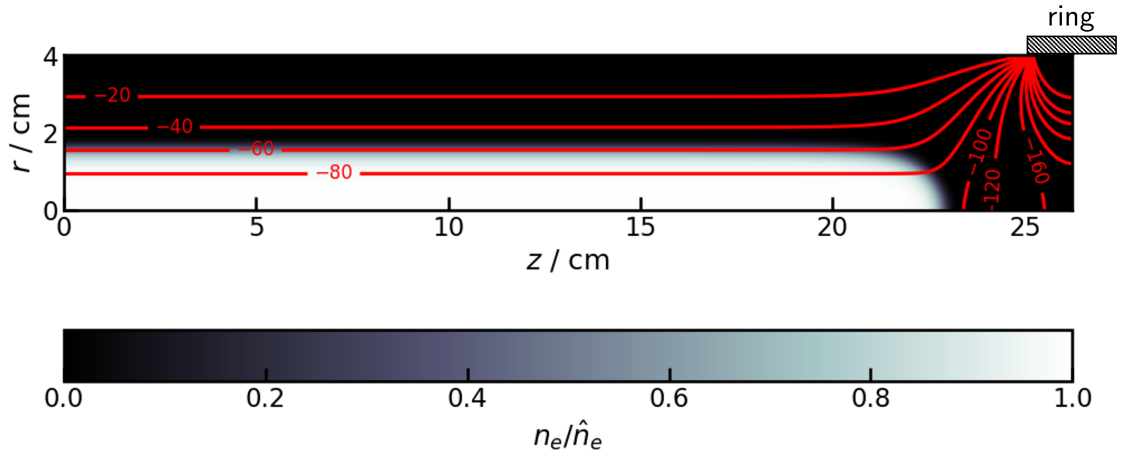

Figure 17: Density distribution of an electron plasma confined by a uniform magnetic field and an electrostatic potential. The right margin coincides with the middle-plane of the gate electrode. The contour lines correspond to constant potentials. The computation domain represents only a quarter of the full geometry. The confining ring is biased to a voltage of $-500\,\mathrm{V}$ and the magnetic field strength is $B = 30\,\mathrm{G}$. The cylinder radius is $a = 4\,\mathrm{cm}$, and the ring lies between $z = 25\,\mathrm{cm}$ and $z = 27\,\mathrm{cm}$. The plasma has a radius $r_p = 1.55\,\mathrm{cm}$ (half-density radius), peak density $\hat{n}_e = 3 \times 10^{13}\,\mathrm{m}^{-3}$, and temperature $T_e = 1\,\mathrm{eV}$.

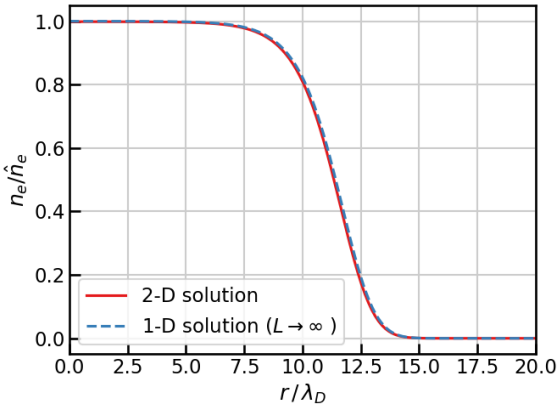

Figure 18: Comparison between the radial density profile $n_e(r, z = 0)$ obtained from the 2-D solution to equation (21) and the 1-D calculation for a plasma column of infinite length L. Both density profiles correspond to thermal equilibrium. The 1-D solution was obtained for a rigid rotation of the plasma column with angular velocity $\omega_{re}/\omega_{re}^- = 1 + 1 \times 10^{-4}$, and a plasma characterised by $2\omega_{pe}^2/\omega_{ce}^2 = 0.6859$ and $\lambda_D = 0.136\,\mathrm{cm}$. The half-density radius $rp = 1.55\,\mathrm{cm}$ extracted from the 1-D solution was used as an input to the 2-D calculation.

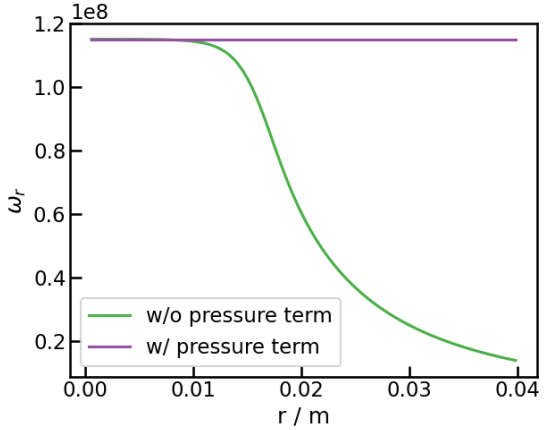

Figure 19: The local angular velocity that corresponds to the plasma density distribution shown in figure 17. The two curves were calculated with the equation (34) with and without the pressure term. When the pressure term is included ($T_e > 0$), the local angular velocity is consistent with a rigid rotation of the plasma column.

temperature T_e, the equilibrium condition is given by [30]

$$m_e n_e \mathbf{v} \cdot \nabla \mathbf{v} = -e n_e \left(\mathbf{E} + \mathbf{v} \times \mathbf{B}\right) - \nabla p, \tag{32}$$

where p is the plasma thermal pressure and for an ideal plasma it is related to temperature by $p = n_e k_B T$. A necessary condition for thermal equilibrium is that the temperature T_e is uniform. The radial component of equation (32) is

$$-m_e n_e \omega_{re}^2 r = -e n_e \left(-\frac{\partial \phi}{\partial r} - \omega_{re} r B\right) - k_B T_e \frac{\partial n_e}{\partial r} \tag{33}$$

which can be rewritten as

$$\omega_{re} = \frac{E_r}{Br} + \frac{k_B T_e}{eBrn_e}\frac{\partial n}{\partial r} + \frac{\omega_{re}^2}{\omega_{ce}}, \tag{34}$$

with $E_r = -\partial\phi/\partial r$, the radial component of $\mathbf{E}$. If the angular velocity ω_{re} is uniform in r (rigid rotation), equation (34) can be integrated to obtain an expression for $n_e(r, z)$ identical to the one in equation (22).

However, when initialising the plasma in a PIC simulation, one has to take into account the absence of elastic collisions between the electrons, and, hence, the absence of thermal pressure. Under this condition, for the plasma not to expand in the few first time steps of the simulation, the velocity distribution has to satisfy equation (34) without a pressure term on the RHS (i.e with T_e set to 0 eV). In the absence of pressure, the velocity distribution does not correspond to a rigid rotation (see figure 19), but it ensures that the plasma column retains its initial density profile throughout the simulation. Therefore, the scheme described in this subsection for initialising the plasma in a simulation allows the control of the shape of the plasma column while it undergoes diocotron motion. Furthermore, the scheme also decreases the total time of a simulation as it removes the requirement for an initial time period when the plasma relaxes from an arbitrary initial shape to a more stable configuration.

4.4 Simulation analysis

The output of the PIC simulation consists of the 6-D phase-space of the macroparticles registered at a regular interval in time which is specified at the beginning of a run. The macroparticles data is further analysed to extract the charge density and information on the plasma temperature based on the phase-space coordinates and weight of each macroparticle.

Furthermore, the three components of the electric field, E_x, E_y, E_z, are registered at each time step at the centre of the storage trap. Due to the diocotron rotation of the plasma column, the transverse components of the electric field, E_x, E_y, exhibit a periodic variation. The diocotron period is, then, obtained by fitting the field variation with a sinusoidal function or by using a Fourier Transform.

Alternatively, the period of rotation of the column was also extracted by calculating the centre of mass position (x_{CoM}, y_{CoM}) of the charge distribution. The centre of mass rotates with the diocotron

frequency, but fewer data points are available from the simulation since the charge distribution was registered at intervals of several hundreds of time steps. Lastly, the total number of physical particles in the simulation domain was recorded as a function of time to evaluate the degree of particle loss.

5 Conclusion

The main two challenges in designing a reliable Gabor lens for LhARA remain the high number of electrons that need to be confined to provide the necessary focusing strength and the stability of the plasma. To address these issues, a set of measurements has been planned to be performed on the positron beamline at the University of Swansea. Even though the beamline is mainly used for studies with positrons, it also allows the storage of electron plasmas. The measurements are intended to inform us of the most suitable techniques to increase the density of the confined plasma for certain externally applied fields and how close to the theoretical limits the density can be increased. Furthermore, measurements of the diocotron drift of an off-axis plasma column are planned to provide experimental data to validate the particle-in-cell (PIC) simulations and the corresponding software. Lastly, a new set of measurements is proposed by studying the focusing effect of a confined electron plasma on a low-energy positron beam.

As a preparation for the measurements, both particle-tracking and PIC simulations have been done. The storage trap and the surrounding beamline at Swansea was modelled and a positron beam was tracked through an idealised, uniform electron plasma. The effect of the external solenoidal magnetic field of the trap and the space-charge field of the plasma is a rotation of the positron beam while passing through the storage trap. Simulations were used to evaluate the magnitude of the rotation in relation to the plasma density and length, and the results were compared to an analytical model based on single particle motion.

For the validation of the PIC software, simulations were performed to model the diocotron rotation of a plasma column around the symmetry axis of the trap. Various methods to initialise the plasma in the simulation have been investigated to ensure low numerical heating and a stable evolution of the diocotron mode. As a result, an initialisation scheme is described which starts from the spatial distribution of a confined plasma in global thermal equilibrium. Such a scheme leads to a low degree of plasma expansion in the initial part of a simulation and provides control on the radius of the plasma from the start.

References

[1] J. H. Malmberg, C. F. Driscoll, B. Beck, D. L. Eggleston, J. Fajans, K. Fine, X. uang, and A. W. Hyatt, "Experiments with pure electron plasmas," *AIP Conference Proceedings*, vol. 175, no. 1, pp. 28–74, 1988.

[2] G. Aymar, T. Becker, S. Boogert, M. Borghesi, R. Bingham, C. Brenner, P. N. Burrows, O. C. Ettlinger, T. Dascalu, S. Gibson, T. Greenshaw, S. Gruber, D. Gujral, C. Hardiman, J. Hughes, W. G. Jones, K. Kirkby, A. Kurup, J.-B. Lagrange, K. Long, W. Luk, J. Matheson, P. McKenna, R. McLauchlan, Z. Najmudin, H. T. Lau, J. L. Parsons, J. Pasternak, J. Pozimski, K. Prise, M. Puchalska, P. Ratoff, G. Schettino, W. Shields, S. Smith, J. Thomason, S. Towe, P. Weightman, C. Whyte, and R. Xiao, "Lhara: The laser-hybrid accelerator for radiobiological applications," *Frontiers in Physics*, vol. 8, p. 432, 2020.

[3] J. Pozimski, R. Dölling, P. Gross, and H. Klein, "Investigation of space charge compensated transport by use of a gabor plasma lens," 01 1996.

[4] M. Droba, B. Glaeser, S. Klaproth, O. Meusel, U. Ratzinger, and K. Schulte, "Studies on Electron Cloud Dynamics for an Optimized Space Charge Lens Design," *Conf. Proc. C*, vol. 110904, pp. 3495–3497, 2011.

[5] K. Schulte, M. Droba, O. Meusel, and U. Ratzinger, "Investigation of diagnostic techniques on a nonneutral plasma," in *Proceedings of the 10th European Workshop on Beam Diagnostics and Instrumentation for Particle Accelerators DIPAC2011, Hamburg, Germany, 2011*, no. MOPD93, pp. 266 – 268, 2011.

[6] P. Posocco, M. Merchant, J. Pozimski, and Y. Xia, "First Test of The Imperial College Gabor (Plasma) Lens prototype at the Surrey Ion Beam centre," in *Proc. of International Particle Accelerator Conference (IPAC'16), Busan, Korea, May 8-13, 2016*, no. 7 in International Particle Accelerator Conference, (Geneva, Switzerland), pp. 1598–1600, JACoW, June 2016.

[7] T. S. Dascalu, "Numerical study of the first gabor lens prototype," Technical Note CCAP-TN-ACCL-05, The Centre for the Clinical Application of Particles (CCAP), Imperial College London, January 2021. `https://ccap.hep.ph.ic.ac.uk/trac/raw-attachment/wiki/Communication/Notes/CCAP-TN-ACCL-05-DASCALU-Titus.pdf`.

[8] "VSim for Plasma," 2020. `https://www.txcorp.com/vsim`.

[9] L. J. Nevay *et al.*, "Bdsim: An accelerator tracking code with particle-matter interactions," *Computer Physics Communications*, p. 107200, 2020.

[10] T. Nonnenmacher, T.-S. Dascalu, R. Bingham, C. L. Cheung, H.-T. Lau, K. Long, J. Pozimski, and C. Whyte, "Anomalous beam transport through Gabor (plasma) lens prototype," *Applied Sciences*, vol. 11, no. 10, 2021.

[11] J. R. Danielson and C. M. Surko, "Torque-balanced high-density steady states of single-component plasmas," *Phys. Rev. Lett.*, vol. 94, p. 035001, Jan 2005.

[12] T. Savage, "Towards non-destructive diagnostics of trapped positrons," Master's thesis, Swansea University, 2019.

[13] M. Knoop, N. Madsen, and R. C. Thompson, *Physics with Trapped Charged Particles*. Imperial College Press, 2014.

[14] J. R. Danielson and C. M. Surko, "Radial compression and torque-balanced steady states of single-component plasmas in penning-malmberg traps," *Physics of Plasmas*, vol. 13, no. 5, p. 055706, 2006.

[15] J. R. Danielson and C. M. Surko, "Torque-balanced high-density steady states of single-component plasmas," *Phys. Rev. Lett.*, vol. 94, p. 035001, Jan 2005.

[16] "Finite Element Method Magnetics (FEMM)." `http://www.femm.info/wiki/HomePage`.

[17] K. S. Fine and C. F. Driscoll, "The finite length diocotron mode," *Physics of Plasmas*, vol. 5, no. 3, pp. 601–607, 1998.

[18] N. C. Hurst, J. R. Danielson, C. J. Baker, and C. M. Surko, "Finite-length, large-amplitude diocotron mode dynamics," *AIP Conference Proceedings*, vol. 1668, no. 1, p. 020003, 2015.

[19] K. S. Fine, "Simple theory of a nonlinear diocotron mode," *Physics of Fluids B: Plasma Physics*, vol. 4, no. 12, pp. 3981–3984, 1992.

[20] H. Fehske, R. Schneider, and A. Weiße, eds., *Computational Many-Particle Physics*. Springer Berlin Heidelberg, 2008.

[21] A. Narimannezhad, C. J. Baker, M. H. Weber, J. Jennings, and K. G. Lynn, "Simulation studies of the behavior of positrons in a microtrap with long aspect ratio," *The European Physical Journal D*, vol. 68, no. 11, p. 351, 2014.

[22] L. Brillouin, "A theorem of larmor and its importance for electrons in magnetic fields," *Phys. Rev.*, vol. 67, pp. 260–266, Apr 1945.

[23] J. H. Malmberg and J. S. deGrassie, "Properties of nonneutral plasma," *Phys. Rev. Lett.*, vol. 35, pp. 577–580, Sep 1975.

[24] R. C. Davidson, *Physics of nonneutral plasmas*. Imperial College Press London, 2001.

[25] S. A. Prasad and T. M. O'Neil, "Finite length thermal equilibria of a pure electron plasma column," *The Physics of Fluids*, vol. 22, no. 2, pp. 278–281, 1979.

[26] T. M. O'Neil and C. F. Driscoll, "Transport to thermal equilibrium of a pure electron plasma," *The Physics of Fluids*, vol. 22, no. 2, pp. 266–277, 1979.

[27] R. L. Spencer, S. N. Rasband, and R. R. Vanfleet, "Numerical calculation of axisymmetric non-neutral plasma equilibria," *Physics of Fluids B: Plasma Physics*, vol. 5, no. 12, pp. 4267–4272, 1993.

[28] R. A. Lane and C. A. Ordonez, "Electrostatic equilibria of non-neutral plasmas confined in a penning trap with axially varying magnetic field," *Physics of Plasmas*, vol. 26, no. 5, p. 052511, 2019.

[29] W. H. Press, S. A. Teukolsky, W. T. Vetterling, and B. P. Flannery, *Numerical Recipes 3rd Edition: The Art of Scientific Computing*. Cambridge University Press, 2007.

[30] J. R. Danielson, D. H. E. Dubin, R. G. Greaves, and C. M. Surko, "Plasma and trap-based techniques for science with positrons," *Rev. Mod. Phys.*, vol. 87, pp. 247–306, Mar 2015.